Abstract. We present a finite difference method for modeling the propagation of electrical waves in cardiac tissue using the cable equation with homogeneous Neumann boundary conditions. This method is novel in that it is derived by first discretizing the phase field method as described by Fenton, et al, then taking a limit to recover a sharp interface. Our method provides for exact voltage conservation (up to floating point precision in application), can be used on arbitrary geometries, and can be implemented using only nearest neighbor coupling between grid points.

SHARP INTERFACE AND VOLTAGE CONSERVATION IN THE PHASE FIELD METHOD: APPLICATION TO CARDIAC ELECTROPHYSIOLOGY

GREGERY T. BUZZARD*, JEFFREY J. FOX†, AND FERNANDO SISO-NADAL‡

Key words. cable equation, Neumann boundary condition, voltage conservation, finite difference, phase field, cardiac model, monodomain

AMS subject classifications. 65M06, 92C30

1. Background. Heart rhythm disorders such as ventricular tachycardia and ventricular fibrillation are a leading cause of morbidity and mortality in the western world. Many researchers have modeled cardiac electrical activity computationally, with the goal of better understanding the mechanisms of such arrhythmias. See, e.g., [17, 18, 20, 21, 22, 25, 26, 28, 30, 31]. Initially, these studies were limited to simple geometries, for which a finite difference method can be expressed in a simple form. Developing more realistic models of cardiac electrical activity presents several challenges. For example, the heart has a complicated 3D geometry, conduction of the electrical wave is anisotropic, and cardiac tissue is made up of cells with heterogeneous electrical properties. Several approaches to the resulting numerical difficulties have been developed. See, e.g., [6, 10, 18, 22, 26, 29, 30]. One method that is particularly simple to implement as a finite difference method in arbitrary geometry using the cable equation is given by Fenton, et al, [8]. Their method is based on a phase field, which is a thin transition layer separating the cardiac tissue from the surrounding medium, typically a passively conducting fluid. As noted by Fenton, et al, the phase field method has been used successfully in several applications, including crack propagation, cellular dynamics, and others. See also [3] for the phase field method used in conjunction with spectral methods.

As described in [8], the implementation of the phase field method on an arbitrary region commences by computing an auxiliary field, ϕ, that describes the cardiac tissue and the transition layer. In their application, $\phi = 1$ in the interior of the heart, decays to 0 across the transition layer, and is 0 in the exterior of the heart. Of course, this necessitates embedding the tissue domain into some larger fictitious domain, usually a rectangular solid. See, e.g., [5] for a discussion and further references for such domain embedding techniques. In [8], the computational domain of the problem is then the region given by $\phi > \epsilon$ for some small ϵ, and this region is typically larger than the original volume of the heart tissue. In compensation for this larger computational domain, the Neumann conditions for no flux across the boundary are said to be

*Purdue University and Gene Network Sciences. Supported in part by NSF grant DMS-0408293. (buzzard@math.purdue.edu),

†Gene Network Sciences. Supported by NIH grants R01 HL075515 and R43 HL077938. (jeff@gnsbiotech.com),

‡Gene Network Sciences. (siso@gnsbiotech.com)

satisfied automatically in the limit as ϵ tends to 0.

In this paper, we use the phase field method to develop a finite difference method that is novel in two ways. The first novelty is that after discretizing the phase field method using positive width transition layer, we take a limit as the transition layer decreases to 0. The discretization of the phase field method involves terms depending on the somewhat artificial function ϕ. Once the discretization has been chosen, we are free to modify ϕ, and we choose to do so to recover exactly the original domain of tissue. Thus, in our formulation, $\phi = 1$ inside the tissue and $\phi = 0$ outside. With this formulation we preserve the ability to handle arbitrary boundary but don't require a larger computational domain. On the other hand, the limiting process converts a strictly finite difference method into a finite difference method for interior nodes plus a linear constraint that captures the homogeneous Neumann condition for boundary nodes. There is some extra computation required to satisfy these boundary conditions, but we show how these conditions can be simplified to produce an implementation in which the value at a boundary node is determined as a weighted average of the values at nearest neighbors. Moreover, the elimination of the transition layer reduces the number of copies of the ionic terms that are required by as much as 40% in models of rabbit ventricles, with a corresponding reduction in simulation time.

The second novelty is that our method gives exact voltage conservation (up to round-off error in practice). That is, in the absence of ionic terms, and assuming homogeneous Neumann conditions, the cable equation conserves voltage in the tissue domain. We show, both analytically and numerically, that these properties are preserved in our discretization. The importance of this property follows from the fact that voltage gain or loss due to numerical inaccuracies in the spatial component may affect the single cell kinetics, leading to inaccuracies in conduction velocity and action potential duration. We also note that this exact voltage conservation property provides a convenient verification of proper implementation.

An alternative approach to voltage conservation would be to use a finite volume method. In some sense, our approach may be considered as a derivative-based analog of the finite volume approach. In the finite volume approach, conservation laws are obtained in a discrete setting by using the average of a given quantity in a rectangular volume, then using the fluxes between adjacent regions to determine the time evolution. These fluxes are typically given in integral form, then must be discretized in some way. Some advantages of this approach are the ability to use unstructured meshes and to handle Neumann boundary conditions relatively easily, although the tensor form that we use still requires some extra effort. In our approach, we start with a differential form of the conservation law, which implies volume conservation via integration by parts. We then apply a discretization designed to yield conservation via the analogous summation by parts (see Section 3). The advantages of this method include the ease of implementation and the ability to handle general boundaries and homogeneous Neumann conditions on a regular grid. For more background on finite difference versus finite volume methods and on domain embedding, see, e.g., [16].

The paper is organized as follows. We first discuss the phase field method as applied to cardiac tissue modeling and examine voltage conservation when using this method. Then we give a derivation of the finite difference method obtained from the phase field method in the limiting case when the transition layer tends to 0 width and show that this gives exact voltage conservation. We also discuss how to implement a computationally efficient discrete version of the homogeneous Neumann boundary conditions. Finally, we describe numerical simulations using this method with atten-

tion to boundary behavior and accurate calculation of local electrical properties such as the velocity of the wave front and the duration of the excitatory period.

We are grateful to the referees and editor for many helpful comments.

2. Discussion of phase field method. As in [23] and others, we ignore mechanical properties of the heart and consider a monodomain model of cardiac electrophysiology in tissue. Although much recent work has focused on the bidomain model in favor of the simpler monodomain model, work of Potse, et al [24] shows that in the absence of externally applied electric fields, the monodomain and bidomain models agree very closely. They conclude that the monodomain model is sufficiently accurate for purposes of studying action potential propagation at the scale of the human heart, and we adopt this view here.

The monodomain model begins with the continuous cable equation

$$\frac{\partial V}{\partial t} = \nabla \cdot D\nabla V - I_{\text{ion}},$$

where V is the membrane potential and I_{ion} is the contribution from the ionic model of a heart cell. Here D is a 3 by 3 diffusion tensor describing the conductivity of the tissue at each point in space. Fenton, et al [8] give a method to determine D based on the fiber direction and the conductivities along fibers and perpendicular to fibers. We assume that the ionic term has been normalized by the membrane capacitance and that D has been adjusted accordingly.

In addition, we impose homogeneous Neumann boundary conditions corresponding to no flux with respect to the diffusion tensor. That is, if R is the region of interest and $\vec{n}$ is the outer normal at a boundary point, then $\vec{n} \cdot D\nabla V = 0$ at each boundary point of R. This implies that there is no current flux normal to the boundary, which implies that in the absence of the I_{ion} term, voltage is conserved. I.e., an application of the divergence theorem to the Neumann condition implies that $\int_R \nabla \cdot D\nabla V d\mu = 0$, where $d\mu$ denotes standard volume measure, so integrating $\partial V/\partial t$ from t_0 to t_1 implies that $\int_R V(t_1)d\mu = \int_R V(t_0)d\mu$ for any times t_0 and t_1.

Following Karma and Rappel [15] and Fenton, et al, [8] we modify the equation above by introducing a phase field to describe the boundary of the desired region. I.e., let ϕ be a smooth function so that the region of interest, R, is given by $R = \{\phi > 0\}$ and so that $\phi = 0$ outside of R and $\phi = 1$ on a large portion of R (note that this differs slightly from the formulation given in the references above but not in a substantive way). The region $\{0 < \phi < 1\}$ is called the transition layer and should be thought of as a thin layer on the inside of the boundary of R. Then the modified equation is

$$\phi \frac{\partial V}{\partial t} = \nabla \cdot (\phi D\nabla V) - \phi I_{\text{ion}}. \tag{2.1}$$

As noted in Fenton, et al, this formulation provides a method for dealing with irregular boundary geometries without requiring extra computational work near the boundary.

In order to understand voltage conservation in this model, we follow the approach in the nonmodified equation and study the behavior in the absence of the ionic term. That is, the ionic term may act as a local source or sink, but without this term the total voltage in the computational domain should be independent of time in the limit as the width of the transition layer tends to 0. Within the region R we have $\phi > 0$, so using the product rule on the right hand side and dividing by ϕ gives

$$\frac{\partial V}{\partial t} = \frac{\nabla \phi}{\phi} \cdot (D\nabla V) + (\nabla \cdot D\nabla V). \tag{2.2}$$

The approximation for voltage conservation (still assuming homogeneous Neumann boundary condition) follows by integrating this expression over R. The integral of the second term is 0 by the divergence theorem exactly as before, while $-\nabla\phi/\|\nabla\phi\|$ should be approximately equal to $\vec{n}$ whenever $0 < \phi < 1$ so that the vectors in the first term are approximately orthogonal. Of course, things are a bit more delicate than this since if ϕ is smooth and 0 outside of R, then Gronwall's inequality implies that $\nabla\phi/\phi$ will be unbounded near the boundary of R.

To understand this more fully, we examine the relationship between voltage conservation and the transition layer, with the goal of showing that as the width of the transition layer tends to 0, the change in total voltage over a fixed time step also tends to 0. For $\epsilon > 0$, let ϕ_ϵ be a function with the properties of ϕ as above, defined so that as ϵ tends to 0, the region $\{0 < \phi < 1\}$ is contained within distance ϵ of the boundary of R. To simplify the exposition, we assume that the region R has smooth boundary, that ϕ_ϵ, V, and D are smooth on the closure of R, and that ϕ_ϵ vanishes to some fixed finite order independent of ϵ at the boundary of R. Given a point q in the boundary of R, we may make a local change of coordinates near q so that $q = 0$ and R is the set of points $p = (x, y, z)$ with $x > 0$ and hence the boundary of R is the set of points with $x = 0$. In this case, $\phi_\epsilon(x, y, z) = (x/\epsilon)^k g_\epsilon(x, y, z)$ for $x \geq 0$, where g_ϵ is a smooth function which is never 0 and k is a positive integer. We assume that $\phi_\epsilon = 1$ when $x \geq \epsilon$ and that $|D_x g_\epsilon|$, $|D_y g_\epsilon|$, and $|D_z g_\epsilon|$ are all uniformly bounded above and g_ϵ is uniformly bounded away from 0, independent of ϵ (e.g., this is true in the case $\phi_\epsilon(x, y, z) = \phi(x/\epsilon, y, z)$).

PROPOSITION 2.1. *With the hypotheses above, there is a constant $C > 0$ so that $\left|\int_R \frac{\partial V}{\partial t} d\mu\right| \leq C\epsilon$.*

Note that we're still assuming $\vec{n} \cdot (D\nabla V) = 0$ on the boundary, so this result is not unexpected. The issue here is the control of the size and direction of the term $\nabla\phi/\phi$ as a substitute for $\vec{n}$.

Proof: A simple calculation with these hypotheses shows that there is a constant $C > 0$ so that at points $p = (x, y, z)$ near 0 with $0 < x < \epsilon$, we have $|D_x\phi_\epsilon/\phi_\epsilon| \leq C/x$. A similar calculation shows that if $q = (0, y, z)$ and $p = (x, y, z)$, then $\|\nabla\phi_\epsilon(p)/D_x\phi_\epsilon + \vec{n}_q\| \leq Cx$ for some (possibly larger) constant $C > 0$ (since the outer normal is $\vec{n}_q = (-1, 0, 0)^T$). Let R_q denote the line of all such p contained in R, and let $R_q(\epsilon)$ denote all such p with $0 < x < \epsilon$. Then adding and subtracting a multiple of $\vec{n}_q$ and using the triangle inequality gives

$$\left|\int_{R_q} \frac{\nabla\phi_\epsilon}{\phi_\epsilon} \cdot (D\nabla V) d\mu\right| \leq \int_{R_q(\epsilon)} \left|\frac{|D_x\phi_\epsilon|}{\phi_\epsilon}\left(\frac{\nabla\phi_\epsilon}{|D_x\phi_\epsilon|} + \vec{n}_q\right) \cdot (D\nabla V)\right| d\mu + \int_{R_q(\epsilon)} \left|\frac{|D_x\phi_\epsilon|}{\phi_\epsilon}\vec{n}_q \cdot (D\nabla V)\right| d\mu.$$

Here we integrated over $R_q(\epsilon)$ since $\nabla\phi_\epsilon = 0$ when $x > \epsilon$. Since $\|D\nabla V\|$ is bounded, the estimates above imply that the first integral on the right is bounded above by $C\epsilon$ for some constant $C > 0$. For the second integral, since D and V are smooth on the closure of R, we have $\|(D\nabla V)_p - (D\nabla V)_q\| \leq C\|p - q\|$. From this and the Neumann condition $\vec{n} \cdot (D\nabla V)_q = 0$, we have

$$\|\vec{n} \cdot (D\nabla V)_p\| = \|\vec{n} \cdot ((D\nabla V)_p - (D\nabla V)_q)\| \leq C\epsilon$$

for $p \in R_\epsilon(q)$. Hence the second integral above is also bounded by $C\epsilon$. Hence using an iterated integral over $q \in \partial R$ and then over R_q, we see that with $\partial V/\partial t$ defined as in (2.2) with ϕ_ϵ in place of ϕ, we have

$$\left| \int_R \frac{\partial V}{\partial t} d\mu \right| \leq C\epsilon$$

for some $C > 0$. ■

The previous proposition implies that in the limit as ϵ tends to 0, and still assuming the given Neumann condition, voltage is conserved. Although this result is reassuring, there are still some delicate issues in terms of computational implementation. In particular, a discretization of (2.2) on a regular grid as outlined in [8] involves calculating weights to be used when updating a grid point based on the values of V at neighboring points. The fact that $\nabla\phi/\phi$ is unbounded near the boundary of the region implies that these weights may become very large near the boundary, affecting either accuracy or stability or both. This problem is circumvented in [8] by choosing a transition layer width that is appropriate for the ionic model under consideration and by ignoring points with small values of ϕ. Due to the decay of ϕ away from R, points inside R affect points outside R more than the reverse. Hence they are able to show that the resulting approximation does not affect the solution significantly. Moreover, they provide a rough argument for how the phase field method maintains an approximation to the Neumann conditions on the boundary. A more detailed argument is given in [3]. However, it is still the case for their algorithm that nodes below cutoff which border nodes above cutoff contribute to the solution but are not determined by the algorithm. If ϕ is small, then the contribution is typically small, but as the width of the transition layer decreases, $\nabla\phi/\phi$ becomes unbounded, leading to large weights. Unless greater attention is given to the boundary condition, the influence of these exterior nodes could frustrate an attempt to increase accuracy by decreasing the width of the transition layer.

In [8], the transition layer is on the order of 4 times the distance between adjacent grid points, with the precise width dependent on the ionic model. For the ionic models used in that paper, this yields a transition layer width between .4mm and 1mm. As mentioned previously, ventricular tissue is made up of nodes with heterogeneous electrical properties. The outer layer of the ventricle, known as the epicardial layer, may be on the same order of 1mm. Since cell heterogeneity plays an important role in arrhythmias [1], an accurate representation of tissue requires reducing or eliminating the transition layer. Additionally, from a computational point of view, a wider transition layer is very costly. In a model of rabbit ventricles (see Section 5), with a grid spacing of .25mm, the phase field method with a transition layer of 4 grid points requires 742790 copies of the ionic model, versus 470196 for the method described here, a reduction of nearly 40%. For a biologically based ionic model, the bulk of simulation time is devoted to the ionic terms, so this corresponds to roughly the same reduction in simulation time.

3. Discretization of phase field method. In this section we derive a finite difference scheme for evaluating the nonionic part of (2.1) on an arbitrary region in a regularly spaced grid in 2 or 3 dimensions (the dimension 1 case is standard). This scheme is based on the limiting case of the phase field method, in which the transition layer has 0 width. That is, the phase field is discontinuous with $\phi = 1$ in R and $\phi = 0$ outside of R. Moreover, this scheme gives exact voltage conservation over the nodes

in R (independent of the values of nodes more than 1 grid space away from R). This conservation property is the most natural analog of the conservation of voltage in the continuous cable equation with homogeneous Neumann boundary conditions and is the most natural requirement for isolated tissue.

The idea of this method is to give a discretization of $\partial V/\partial t = \nabla \cdot (\phi D \nabla V)$ so that the sum of the spatially discretized formula for $\partial V/\partial t$ over all space is 0. This approach is motivated by the corresponding result in the continuous case. That is, if $\partial V/\partial t = \nabla \cdot (\phi D \nabla V)$, (instead of $\phi \partial V/\partial t$ on the left as in (2.1)), then $\int_R V_t d\mu = 0$ even in the absence of any boundary conditions. To see this, we use integration by parts: Since $\phi = 0$ outside of R we may integrate over all of space and apply the product rule to get

$$\int_R \nabla \cdot (\phi D \nabla V) d\mu = \int_{\mathbb{R}^n} (\nabla \phi) \cdot (D \nabla V) d\mu + \int_{\mathbb{R}^n} \phi (\nabla \cdot D \nabla V) d\mu, \tag{3.1}$$

where n may be 1, 2, or 3. We next apply integration by parts. Again since $\phi = 0$ outside of R (which we assume to be bounded), the boundary terms evaluate to 0, so the first term in the right hand side of the previous equation is

$$-\int_{\mathbb{R}^n} \phi (\nabla \cdot D \nabla V) d\mu.$$

Hence the two integrals cancel to give 0 and hence voltage conservation.

The discretized version of this conservation result is motivated by the formula for summation by parts that is the analog of integration by parts as described in Graham, et al, [12]. In the simplest case, define $\Delta f(x) = f(x+1) - f(x)$, where x is restricted to a discrete grid. The summation by parts formula can then be written in indefinite form as

$$\sum u \Delta v = uv - \sum (Ev) \Delta u,$$

where E is the operator such that $Ev(x) = v(x+1)$. For our purposes, we will sum over an infinite grid, and our functions will have bounded support, so in this case we have the formula

$$\sum_x u(x) \Delta v(x) = -\sum v(x+1) \Delta u(x).$$

To use this idea to convert the continuous differential expression $\nabla \cdot (\phi D \nabla V)$ into a discrete expression, we first expand in terms of partial derivatives. Letting D_{ij} denote the (i,j)th entry of D, and letting ϕ_{x_j} denote the partial derivative of ϕ with respect to x_j, etc., we have

$$\nabla \cdot (\phi D \nabla V) = \sum_{i,j=1}^{3} \left(\phi_{x_i} D_{ij} V_{x_j} + \phi (D_{ij})_{x_i} V_{x_j} + \phi D_{ij} V_{x_i x_j} \right). \tag{3.2}$$

There are various choices for discretizing the spatial derivatives. Here we make these choices so that the discretization of (3.2) is accurate to $O(\|\Delta x\|^2)$ on a regular grid with grid spacing $\Delta x = (\Delta x_1, \Delta x_2, \Delta x_3)$ and so that the sum of (3.2) over $\mathbb{R}^3$ is 0. That is, we seek to reproduce exact voltage conservation in the discrete case, just as summation by parts reproduces integration by parts as indicated above.

We assume that the problem lies on a regularly spaced grid that is infinite in all directions with a point described as $p = (x_1, x_2, x_3)$ (the 2-dimensional case will be obtained simply by ignoring the third dimension). The grid space in the ith coordinate direction is Δx_i, and e_i represents the vector that is Δx_i in the ith coordinate and 0 in the other coordinates. Given a function, f, defined on the grid, and given a grid point, p, define

$$\begin{aligned}
\Delta_i f(p) &= \frac{f(p+e_i) - f(p)}{\Delta x_i} \\
\bar{\Delta}_i f(p) &= \frac{f(p+e_i) - f(p-e_i)}{2\Delta x_i} \\
\Delta^i_j f(p) &= \begin{cases} \Delta_i f(p) & \text{if } i = j \\ \frac{1}{2}(\bar{\Delta}_j f(p) + \bar{\Delta}_j f(p+e_i)) & \text{if } i \neq j \end{cases} \\
\Delta_{ij} f(p) &= \begin{cases} \Delta_i \Delta_i f(p-e_i) & \text{if } i = j \\ \bar{\Delta}_i \bar{\Delta}_j f(p) & \text{if } i \neq j \end{cases} .
\end{aligned}$$

The first two of these definitions are standard discretizations of first derivatives, which are first and second order accurate, respectively. The third definition is a discretization of a first derivative that is tuned to provide necessary cancellations for the conservation result that we seek, and the final definition is a standard discretization of a second derivative in the nonmixed and mixed cases, respectively.

Using these definitions, and using $V_t(p)$ to denote the change in $V(p)$ (using either continuous or discrete time), the spatially discrete analog of (2.1) without the ionic term is

$$\begin{aligned}
\phi(p)V_t(p) = \sum_{i,j=1}^{3} \Big[& \frac{\phi(p)}{2}(\Delta_i D_{ij}(p)\Delta^i_j V(p) + \Delta_i D_{ij}(p-e_i)\Delta^i_j V(p-e_i)) \\
& + \frac{D_{ij}(p)}{2}(\Delta_i \phi(p)\Delta^i_j V(p) + \Delta_i \phi(p-e_i)\Delta^i_j V(p-e_i)) \\
& + \phi(p) D_{ij}(p)\Delta_{ij} V(p)\Big].
\end{aligned} \tag{3.3}$$

The primary novelty in this discretization is in the first two terms, where the product of derivatives, $f_{x_i} g_{x_j}$, is approximated using $(\Delta_i f(p)\Delta^i_j g(p) + \Delta_i f(p-e_i)\Delta^i_j g(p-e_i))/2$. When $i = j$, this expression is symmetric in f and g, while if $i \neq j$, it is not symmetric in f and g. However, we show later that in either case it is accurate up to $O(\|\Delta x\|^2)$. Note also that if p has distance more than 1 from R, then $\phi(p) = 0$ and $\Delta_i \phi(p) = 0$, so the right hand side is 0.

As noted above, the motivation for this expression is to provide exact voltage conservation in analogy with the fact that the left hand side in (3.1) evaluates to 0. We demonstrate this property below.

PROPOSITION 3.1. *Let $Q(p)$ denote the right hand side in* (3.3). *Then* $\sum_p Q(p) = 0$.

Proof: We show that for each fixed i and j, the sum over all p of the corresponding terms of $Q(p)$ gives 0. We distinguish 2 cases: $i = j$ and $i \neq j$. In both cases, we use the fact that we can change the index of summation at will since we sum over all possible p. In the case $i = j$, we apply this to the last term in the second

line of (3.3) by expanding $\Delta_i\phi(p-e_i)$ and converting $p-e_i$ to p to get

$$\begin{aligned}\sum_p \frac{D_{ii}(p)}{2}\Delta_i\phi(p-e_i)\Delta_i^i V(p-e_i)&\\ &= \sum_p \frac{D_{ii}(p)}{2}\left(\frac{\phi(p)-\phi(p-e_i)}{\Delta x_i}\right)\Delta_i^i V(p-e_i)\\ &= \sum_p \frac{\phi(p)}{2\Delta x_i}D_{ii}(p)\Delta_i^i V(p-e_i) - \sum_p \frac{\phi(p)}{2\Delta x_i}D_{ii}(p+e_i)\Delta_i^i V(p).\end{aligned}$$

The first sum on the last line combines with a similar sum obtained from the first term of the second line of (3.3) to give $-\sum_p \phi(p)D_{ii}(p)\Delta_i V(p-e_i)/\Delta x_i$, while the second sum on the right is canceled by a sum from the first term of the first line of (3.3). Similar operations on the remaining terms imply that after summing over all p, the first two lines of (3.3) exactly cancel the last line in the case $i=j$.

The case $i\neq j$ follows using a similar argument, although the calculations are more tedious. Since the method is essentially mechanical, we omit the details. However, together, these results show that $\sum_p Q(p)=0$, as desired. ■

We verify next the order of accuracy of the numerical scheme described above.

PROPOSITION 3.2. *Let f and g be smooth functions in $\mathbb{R}^2$. Then*

$$\frac{1}{2}(\Delta_i f(p)\Delta_j^i g(p) + \Delta_i f(p-e_i)\Delta_j^i g(p-e_i)) = f_{x_i}(p)g_{x_j}(p) + O(\|\Delta x\|^2).$$

Moreover, (3.3) *is a $O(\|\Delta x\|^2)$-accurate approximation of* (2.2).

Proof: From the definition of Δ_i and standard results, we have

$$\Delta_i f(p) = f_{x_i}(p) + \frac{f_{x_ix_i}(p)}{2}\Delta x_i + O(|\Delta x_i|^2),$$

while

$$\Delta_i f(p-e_i) = f_{x_i}(p) - \frac{f_{x_ix_i}(p)}{2}\Delta x_i + O(|\Delta x_i|^2).$$

Also

$$\Delta_j^i g(p) = g_{x_j}(p) + \frac{g_{x_ix_j}(p)}{2}\Delta x_i + O(\|\Delta x\|^2),$$

and there is a similar expression for $\Delta_j^i g(p-e_i)$, with $-\Delta x_i$ in place of Δx_i (if $i=j$, this is standard, while if $i\neq j$, it follows from $(\Delta_j^i g(p) = \frac{1}{2}(g_{x_j}(p) + g_{x_j}(p+e_i)) + O(|\Delta x_j|^2))$. Using these expressions in the left hand side of the formula in the statement of the proposition and collecting terms proves the first statement. The second statement follows from the first plus the fact that the discretizations used in (3.3) for the second derivatives are known to be second order accurate. ■

Note that $V_t(p)$ depends only on the values of ϕ, D, and V at the nearest neighbors of p obtained by changing one or two coordinates of p by one grid space. Hence $V_t(p)$ can be expressed as a weighted sum of the values of V at the nearest neighbors of p.

4. Boundary behavior. As before, let $Q(p)$ denote the right hand side of equation (3.3), so that $\phi(p)V_t(p) = Q(p)$. In the limiting case of $\phi = 1$ in R and $\phi = 0$ outside of R, this reduces to $V_t(p) = Q(p)$ in R (a formula for updating $V(p)$) and $Q(p) = 0$ outside of R (a constraint that must be satisfied for consistency). Moreover, at any point p such that both $\phi(p) = 0$ and $\phi(p \pm e_i) = 0$ for each i, we have $Q(p) = 0$. Hence in this case the consistency constraint is satisfied automatically. However, there are points p with $\phi(p) = 0$ but $\phi(p \pm e_i) \neq 0$ for some i. Let $B(R)$ denote the set of such points, and call any point in $B(R)$ a boundary point. In order to satisfy the consistency constraint $Q(p) = 0$, we need to set the value of V at each boundary point p so that $Q(p) = 0$.

Note that the constraint $Q(p) = 0$ is simpler than it first appears since if $p \in B(R)$, then $\phi(p) = 0$, so $Q(p)$ simplifies to

$$\hat{Q}(p) = \sum_{i,j=1}^{3} \frac{D_{ij}(p)}{2}(\Delta_i\phi(p)\Delta_j^i V(p) + \Delta_i\phi(p - e_i)\Delta_j^i V(p - e_i)),$$

which is a discretization of $(\nabla\phi) \cdot (D\nabla V)$. As noted above, $-\nabla\phi/\|\nabla\phi\|$ can be considered as an approximation to the outer normal near the boundary of R, so $\hat{Q}(p) = 0$ is a discrete approximation to the Neumann condition. Thus, we propose the following analogy.

ANALOGY 4.1. *Let R be an open region with smooth boundary in $\mathbb{R}^n$, $n = 1, 2, 3$. Then the nonionic part of the continuous cable equation with homogeneous Neumann boundary conditions is*

$$\begin{cases} \frac{\partial V}{\partial t}(p) &= (\nabla \cdot D\nabla V)(p) & \text{if } p \in R \\ \vec{n}(p) \cdot (D\nabla V)(p) &= 0 & \text{if } p \in \partial R \end{cases}$$

Fix a regular grid as above, let $Q(p)$ equal the right hand side in (3.3), let $\hat{Q}(p)$ denote the simplification of $Q(p)$ given above, let ϕ be the characteristic function for R, so that $\phi = 1$ in R and $\phi = 0$ everywhere else, and let $B(R)$ denote the boundary points of R as described above. Then the (semi)discrete analog of the cable equation is

$$\begin{cases} V_t(p) &= Q(p) & \text{if } p \in R \\ \hat{Q}(p) &= 0 & \text{if } p \in B(R) \end{cases}$$

The equation $\hat{Q}(p) = 0$ produces one equation for each p in $B(R)$, and this equation is linear in $V(p)$. Note that the set of all such equations has the form $A\vec{v} = B\vec{u}$, where A is determined only by D and ϕ, and where B is determined by D and ϕ, and $\vec{u}$ is given by the values of V in R.

In order to evaluate $\hat{Q}(p)$, we need to know the values for D at points in $B(R)$. Since these points lie outside of R, the choice of value is somewhat arbitrary. We calculate D here based on an extension of fiber direction to $B(R)$. Fenton, et al [8] show that $D = D_\perp\mathbf{I} + (D_\parallel - D_\perp)\mathbf{f}\mathbf{f}^T$, where $\mathbf{f}$ is the fiber direction and $D_\parallel$ and $D_\perp$ are the parallel and perpendicular conductivities, respectively.

From this formula for D, there are at least two natural ways to determine D on $B(R)$. One method is to extend the fiber directions to $B(R)$ as an average of neighboring fiber directions, then using these directions to determine D as was done in R. With this approach, there will generally be more unknowns than equations:

there is one equation for each p in $B(R)$, but in addition to the unknowns $V(p)$ for each such p, there are also unknowns of the form $V(p)$ where p is outside R, $p \pm e_i$ is outside R for each i, but some $p \pm e_i \pm e_j$ is in R. The conservation property holds independently of the choice of value for such points. In order to minimize any possible effect from these points, we set them to be the average of nearest neighbors that lie in R. This method leads to a matrix equation $A\vec{v} = B\vec{u}$ which can be solved for $\vec{v}$ using a sparse linear solver. In practice, for anisotropic domains with varying fiber directions and with a ratio of fiber diffusion to perpendicular diffusion on the order of 5 to 1, the condition number of A is less than 100 and the norm of B is less than 20. This is true for all of the examples in Section 5. Thus, this system is easily solvable in practice. One drawback of this method is that the value of $V(p)$ at a particular point will usually depend on values of V at points more than one grid space away.

A second method for choosing D is designed to minimize the computation involved at each time step. Note that if $\mathbf{f}$ is parallel to one of the axes (i.e., has only one nonzero coordinate), then $D(p)$ is diagonal with positive entries on the diagonal (assuming $D_\parallel$ and $D_\perp$ are positive). In this case, the equation $\hat{Q}(p) = 0$ reduces to

$$\sum_{i=1}^{3} \frac{D_{ii}(p)}{2}(\Delta_i\phi(p)\Delta_i V(p) + \Delta_i\phi(p-e_i)\Delta_i V(p-e_i)) = 0.$$

With $p \in B(R)$ and hence $\phi(p) = 0$, this simplifies to

$$CV(p) = \sum_{i=1}^{3} \frac{D_{ii}(p)}{2\Delta_i^2}(\phi(p+e_i)V(p+e_i) + \phi(p-e_i)V(p-e_i)), \tag{4.1}$$

where C is a positive constant. In particular, aside from $V(p)$, all other $V(q)$ that appear in this equation with nonzero coefficients have $\phi(q) = 1$, hence lie inside R, hence have known value. Thus, the value of $V(p)$ can be determined directly as a weighted sum of the value of V at the nearest neighbors of p without solving a large linear system. To determine $\mathbf{f}$, we use the averaging process described for the first method, then project to one of the coordinate axes, either the closest axis or one of the axes chosen according to a probability distribution based on the components of the unprojected vector. Note that this method is the same as the first method in the isotropic case and that this method does not make any changes to the fiber directions in the interior of R. Only points on the boundary are affected. As we will see in Section 5, this method gives up some accuracy in return for lower computational cost, but in realistic geometry with varying fiber direction, the loss is quite small.

Finally, note that in either case, the unknown voltages are linear functions of the voltages in R, and both the known and unknown voltages appear linearly in (3.3). Hence the spatial terms without ionic influence (which are integrated separately in a decoupled scheme described below) can be written in the form $V_t = AV$, where V is the vector of voltages for points in R and A is a constant matrix.

5. Implementation and numerical results. The algorithm we used for the results below is based on an operator splitting approach in which the ionic terms are integrated independently for a time step Δt, after which the spatial component is integrated for the same time step using these values. We used a stiff solver (the CVODE solver from http://acts.nersc.gov/sundials/ using backwards differentiation) for the ionic terms and a second-order approximation of the matrix exponential for the spatial update. As mentioned above, the spatial terms have the form $V_t = AV$, where

A is a constant matrix, so the solution can be found as $V(t+\Delta t) = \exp(AV(t)\Delta t)$. In practice, the matrix exponential is difficult to compute accurately [19], but packages such as expokit [27] can be used even in the case of large, sparse matrices A as found here in the case of realistic geometry. We chose a simpler method here to insure voltage conservation and to limit the amount of communication required between grid points. With this approach in the case of boundary fibers projected to coordinate axes, the spatial update for a given time step requires information from points at most 2 grid spaces away from a given point and hence is easily parallelizable. Note that an alternative implementation using the method of lines without operator splitting can be obtained by adding V_t to the ionic terms. This yields a stiff system of ODEs which can be solved using CVODE (or other packages) with appropriate preconditioning. This gives a significant decrease in computation time, but since our focus here is on the voltage conservation property, we used operator splitting in order to isolate the spatial contribution.

To define the fiber directions at boundary points, we start with fiber directions at points in R, then determine the fiber direction at p in $B(R)$ by taking an average of the directions of nearest neighbors. In the simplified case described above, we then project this onto the nearest coordinate axis (or select one axis in the case of a tie). In either case, $D(p)$ is calculated as indicated above, then this information is used to determine the weights to be used in solving (4.1).

For the integration itself, we start with $V(p,t)$ and integrate the ionic term for each p in R for a time step Δt to obtain a value $U(p, t + \Delta t)$. Then we use a second order approximation to the matrix exponential to compute the vector of values $V(t + \Delta t) = (I + M\Delta t + M^2(\Delta t)^2/2)U(t + \Delta t)$, where M is the constant matrix described at the end of the previous section.

We examine our method on several different domains and compare it to the phase field method and, in cases with simple boundary and constant fiber orientation, to a standard, symmetric, second order finite difference scheme. In particular, we focus on action potential duration (APD) and conduction velocity in simple domains for the canine ventricular model (CVM) of Fox, et al, [11] and compare results using the method given here to results using the phase field method and the standard method. We then show results in more realistic geometry using the 3 variable phenomenological model of [7] as well as CVM, again comparing the method given here to the phase field method. Here and throughout, the 3 variable model refers to the 3 variable model of [7] with parameter set 5 of that paper.

Our implementation of the phase field method also uses operator splitting with the same integration methods for ionic and spatial terms as described above. To determine the phase field, we use a convolution as in [3] with a cutoff of 10^{-4}. As mentioned in [8], the precise form of the phase field profile is not critical to the algorithm; however, different profiles may yield differing results, which may explain the sensitivity of the results to the boundary cell values that is reported below.

As shown in Figure 5.1, the conduction velocity of CVM is much more sensitive to spatial resolution than is the 3 variable model. For this reason, we studied conduction velocity using CVM with a spatial resolution of .01cm in each direction and a time step of .005ms. We used a 2 dimensional domain of length 4cm and height .2cm with a centered rectangular hole of length 2.5cm and height .08cm, all fibers oriented in the $(1, 1)$ direction and diffusion coefficient of 1 cm^2/s in the fiber direction and .2 cm^2/s in the perpendicular direction. We used the published version of CVM as in [11] with identical initial conditions (as published) for all grid points. We stimulated

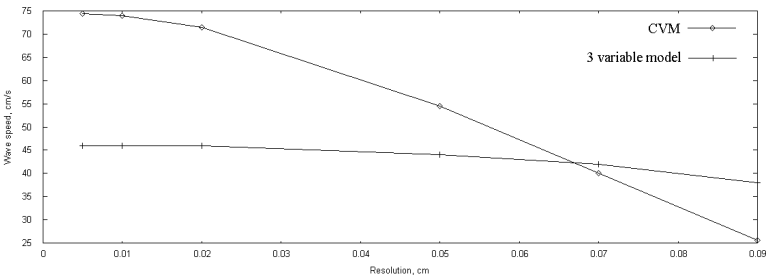

FIG. 5.1. *Dependence of conduction velocity on grid resolution for CVM and the 3 variable model. The steeper curve represents CVM and the flatter curve represents the 3 variable model. These calculations were done in a 1-dimensional fiber of length 2cm using a diffusion coefficient of 1 cm^2/s. In each case, the time step, Δt, was chosen to satisfy $\Delta t < 25(\Delta x)^2$. Reducing Δt below this value produced no significant change in conduction velocity.*

the rightmost .2cm of the strip with a square pulse of amplitude 80mV and duration 1ms, then recorded the voltage trace at two grid points: one at the lower left corner corner of the hole (inside corner) and one at the lower left corner of the strip (outside corner). We repeated this simulation using 6 different methods: (a) sharp interface method with boundary fibers also in the $(1, 1)$ direction, (b) sharp interface method with boundary fibers projected to the $(1, 0)$ direction, (c) phase field method with grid points below cutoff (we call these 'exterior points' in the sequel) set to the average of nearest neighbors, (d) phase field method with exterior points set to 0mV, (e) phase field method with exterior points set to -94mV (the approximate rest potential for CVM), (f) a standard symmetric second order finite difference scheme for comparison. For the phase field method, we used a transition layer of 4 grid points. As mentioned after proposition 2.1, grid points below cutoff which border the transition layer still affect the simulation, and it is these nodes which we set in the three different ways in (c)-(e).

With these conditions, Panel (c) of Figure 5.2 shows the position of the wavefront using the voltage conservation method without boundary fiber projection. The lines shown give the position of the wavefront at 10ms intervals, starting with the rightmost curve at 1ms. Note that the rightmost curve is nearly vertical since the stimulus was applied to the rightmost .2cm of the strip; however, the anisotropy causes the wavefront to align quickly with the fiber direction. The other methods give nearly identical isochrone pictures with differences only in the conduction velocity, which are detailed in Panel (a). The upper figure in Panel (a) shows the voltage traces recorded at the lower left corner of the rectangular hole while the lower figure shows the traces recorded at the lower left corner of the strip. The time of the upstroke at this latter point determines the travel time of the wave over the 3.8cm between the leading edge of the stimulus and the point of recording. This figure shows that all 6 methods have a travel time in the range of 81ms to 85ms, which corresponds to average wave speeds in the range of .44 to .46 m/s. For both sets of recordings, the sharp interface method using projection and the phase field method with exterior points set to 0mV give the smallest travel time while the phase field with exterior points set to -94mV gives the largest travel time. The sharp interface method without fiber projection, the phase field method with exterior points set to the average of neighbors, and the standard method all agree closely at both points of recording. Note that conduction velocity is slower in this figure than in Figure 5.1 because the propagation of the wave

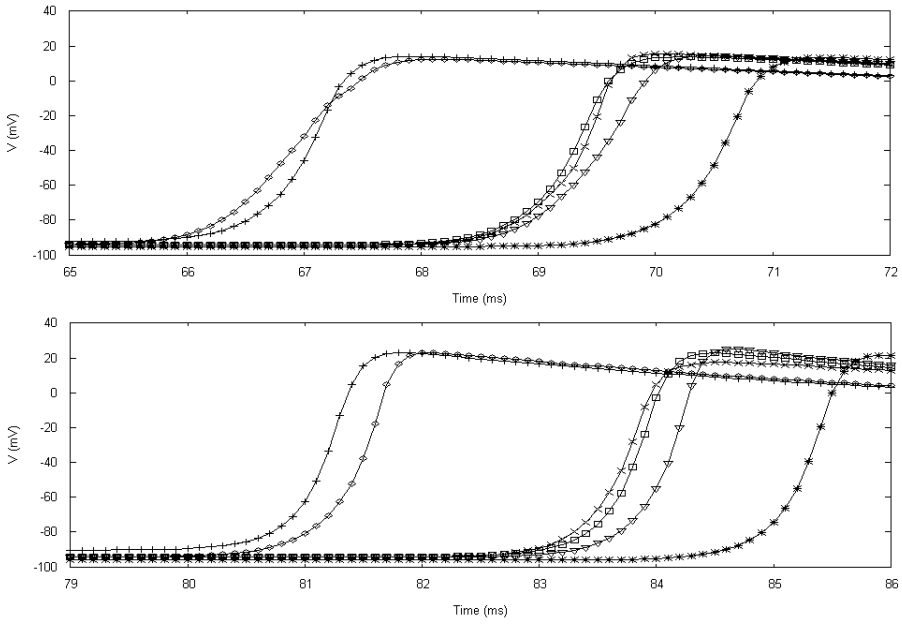

(a) Voltage traces at lower left inside corner (upper figure) and lower left outside corner (lower figure).

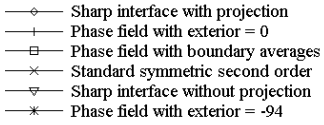

(b) Legend for voltage traces.

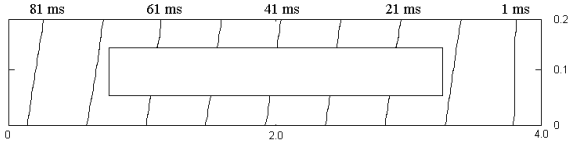

(c) Isochrones using sharp interface method without boundary projection. The wave is travelling right to left.

FIG. 5.2. *(a) Voltage traces recorded at the lower left inside corner and lower left outside corner, respectively of the region shown in (c). (b) Legend for part (a). (c) Isochrones for the standard symmetric second order finite difference method. Each line represents the position of the wavefront at a given time, with adjacent lines 10ms apart. The wavefront is moving right to left in a 2 dimensional domain of size 4.0cm by .2cm with a centered rectangular hole of size 2.5cm by .08cm. The spatial resolution is .01cm. The tissue was stimulated on the right end (x range between 3.8cm and 4cm) for 1ms, after which time the wavefront is given by the nearly vertical line at the right. The remaining wavefronts are aligned with the fiber orientation of* $(1, 1)$. *The isochrones for the other methods look nearly identical up to scaling in the x direction to account for differences in average wave speed.*

is essentially in the direction perpendicular to the fiber, for which diffusion is only $.2\text{cm}^2/s$.

For these simulations, the maximum change in total voltage due to the spatial update in one time step was less than 2.3×10^{-8} mV for the two voltage conservation methods, was 1.7mV for the standard symmetric method, was more than 18mV for the phase field method using the average method and was more than 1200mV for the phase field method using either of the two constant value methods. Even so, the worst of these represents an average gain or loss of less than 1.5mV per boundary cell, when action potential amplitude for this model is more than 90mV. For purposes of conduction velocity, any of these methods give reasonable results, although the sharp

interface method requires only 6260 grid points versus more than 11000 for the phase field method. Since the ionic terms require the bulk of processor time, this ratio is largely preserved in terms of compute time also.

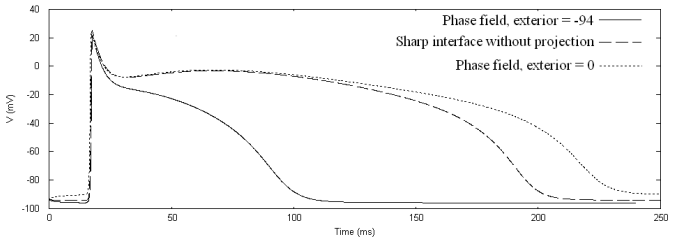

(a) Voltage traces at lower left corner.

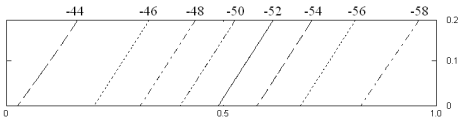

(b) Voltage level curves for sharp inteface, no projection.

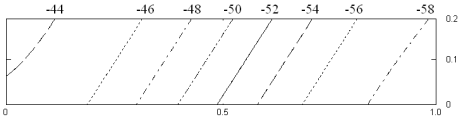

(c) Voltage level curves for sharp inteface, with projection.

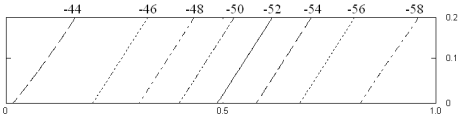

(d) Voltage level curves for phase field using boundary averages.

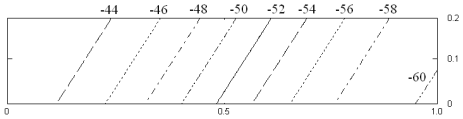

(e) Voltage level curves for standard second order differences.

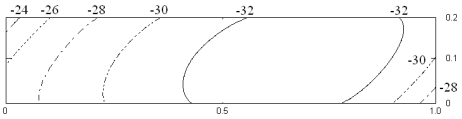

(f) Voltage level curves for phase field with exterior = 0.

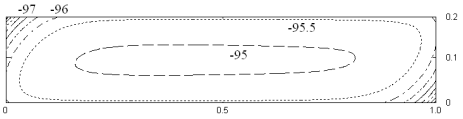

(g) Voltage level curves for phase field with exterior = -94.

FIG. 5.3. *Comparison of the behavior of repolarization in a strip of size 1.0cm by 0.2cm, fibers oriented in the (1,1) direction, stimulated for 1ms on the rightmost .2cm of the strip. (a) Voltage traces as measured in the lower left corner of the strip for the sharp interface method without boundary fiber projection plus the phase field method with exterior points set to 0 and -94. The phase field method with boundary averages and the sharp interface method with projection produce traces nearly identical to the middle trace. The standard second order method produces a trace which is nearly identical to the middle trace except for a 1ms delay in repolarization. (b)-(g) Voltage level curves at 175ms for the methods indicated. The voltage in mV is indicated next to the corresponding level curve. Note the difference in both shape and range of values for (f) and (g) as compared to the other methods.*

To study the dependence of the APD on the integration method, we used a strip of length 1.0cm and height 0.2cm (see Figure 5.3). We stimulated the rightmost 0.2cm as above using each of the 6 methods described above, then recorded the voltage trace at a node on the opposite end of the strip. In this case, both versions of the sharp interface method and the phase field method with averages on the boundary produced

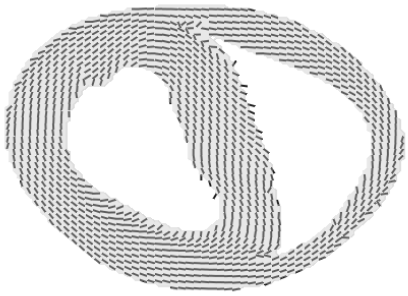

(a) Fiber orientations in a slice of rabbit ventricles.

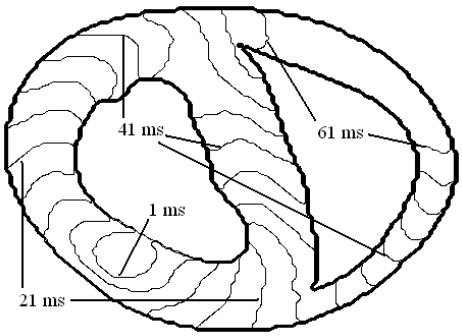

(b) Isochrones using sharp inteface method with projection.

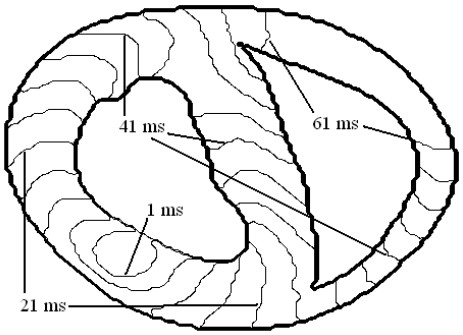

(c) Isochrones using sharp inteface method without projection.

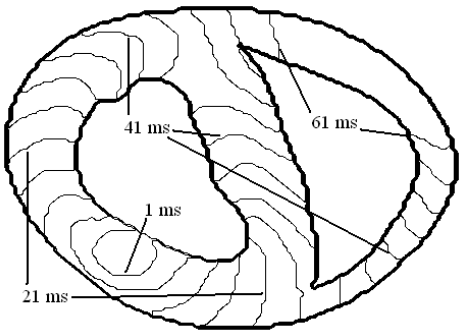

(d) Isochrones using phase field method with boundary averages.

FIG. 5.4. *(a) The domain and fiber orientation for simulations on a slice of rabbit ventricles. (b) Isochrones indicating the position of the wavefront at 5ms intervals for the voltage conservation method without boundary fiber projection. The tissue was stimulated for 1ms in a disk in the lower left of the domain. Each isochrone shows the position of the wavefront at the corresponding time. (c) Isochrones for the voltage conservation method with fiber projection. (d) Isochrones for the phase field method with averages on the boundary.*

nearly identical results. The standard symmetric second order method yielded a trace that is nearly the same except for a 1ms delay in repolarization. This trace is not shown in (a) of Figure 5.3 but the delay is evident in (e). Even so, the agreement between (b)-(e) in Figure 5.3 is quite close. However, as shown in the voltage trace (a) in Figure 5.3 and the level sets (f) and (g) in the same figure, the constant boundary values in the remaining two phase field methods have a significant impact on APD. When the boundary values are set to 0mV, they act as voltage sources, cause neighboring nodes to produce a lengthened APD. Likewise, when set to -94mV, they act as sinks, causing APDs throughout the domain to be shortened considerably. As mentioned previously, this sensitivity may in part be due to the particular choice of the phase field profile.

To give an indication of the ability to handle more general geometry with varying fibers, we simulated wave propagation on a slice of rabbit ventricles using the 3 variable model of [7] (parameter set 5) with a spatial resolution of 0.25mm and a time step of .01ms. The domain and fiber directions are shown in Figure 5.4. The tissue was

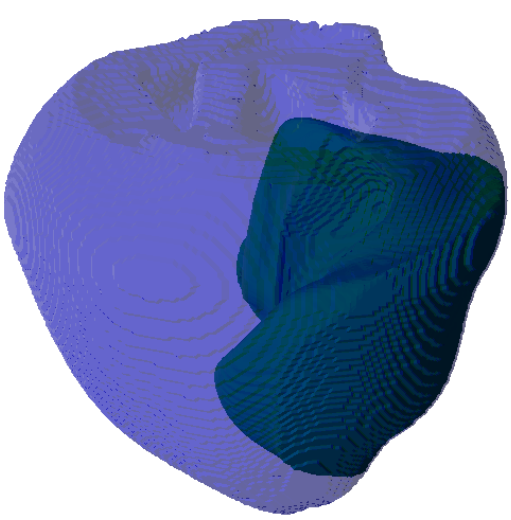

(a) Spreading activation wave in rabbit ventricles.

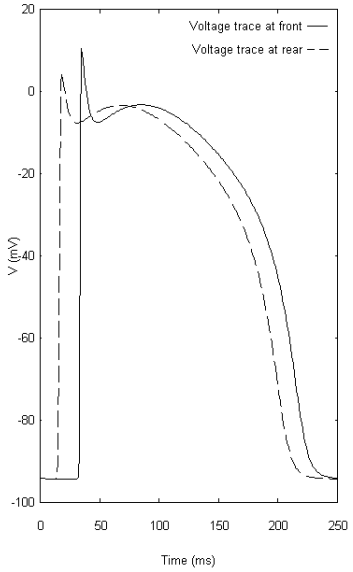

(b) Voltage traces as recorded at the front and rear as viewed from the perspective in Panel (a).

FIG. 5.5. *(a) Spreading activation wave in the full rabbit ventricles using the voltage conservation method with projection of boundary fibers. The spatial resolution is 0.25mm in each direction, and the cell model is CVM. The tissue was stimulated for 1ms in a box of size 0.2cm by 0.2cm by 0.1cm located in the middle right and slightly to the rear as seen from this angle. This figure shows the wavefront after 30ms. (b) Voltage traces as recorded at the vertical middle at positions in the front and rear as viewed from the angle in Panel (a). These traces shows that the action potential propagates and repolarizes as expected, even with the anisotropy in 3 dimensions. The difference in time of upstroke is due to the position of the stimulus relative to the point of recording.*

stimulated for 1ms with an amplitude of 80mV in a circular region in the lower left in each figure. Given the results above on APD and conduction velocity, we excluded the phase field method with exterior cells held fixed. Also, we excluded the standard symmetric method since it is not clear how to implement it for arbitrary boundary and nonconstant fiber orientation. Hence we considered only the remaining 3 methods. All 3 methods show very good agreement in terms of wave propagation and repolarization. In this case, the voltage conservation methods required only 4727 grid points versus 7160 for the phase field method. Also, the voltage conservation methods yielded a maximum total voltage change on any given step of 7.3×10^{-11} mV, versus 0.18 mV for the phase field method.

Finally, Figure 5.5 shows a wave propagating in a model of rabbit ventricles, using CVM with a spatial resolution of 0.25mm, time step of .01ms, and boundary fibers projected to coordinate axes. The tissue was stimulated in a box of size 0.2cm x 0.2cm x 0.1cm on the lower right for 1ms. This figure shows the wavefront after 30ms. This simulation required 470197 grid points, versus 742790 for the phase field method. We are grateful to Wouter-Jan Rappel for provided the fiber orientation data used in Figures 5.4 and 5.5.

6. Conclusion. We presented a finite difference method for modeling the propagation of electrical waves in cardiac tissue using the cable equation with homogeneous Neumann boundary conditions. The novelty of this method comes from the application of a limiting process only after a discretization has been applied to the phase field method. In so doing, we reduce the size of the compuational domain relative to the phase field method and we obtain exact voltage conservation in the absence of ionic terms (up to floating point precision in application). Moreover, our method can be easily used on arbitrary geometries, and can be implemented using only nearest neighbor or second nearest neighbor coupling between grid points, making it very easy to implement in a parallel fashion.

REFERENCES

[1] C. Antzelevitch, W. Shimizu, "Cellular mechanisms underlying the long QT syndrome," Curr. Opin. Cardiol. 17 (2002), pp. 43-51.

[2] V.N. Biktashev, A.V. Holden, and H. Zhang, "Tension of organized filaments of scroll waves," Philos. Trans. R. Soc. London, Ser. A, 347 (1994), pp. 611-630.

[3] A. Bueno-Orovio, V.M. Perez-Garcia , and F.H. Fenton, "Spectral methods for partial differential equations in irregular domains: the spectral smoothed boundary method," Siam J. Sci. Comput., 28, (2006), pp. 886-900.

[4] M. Courtemanche and A.T. Winfree, "Re-entrant rotating waves in a Beeler-Reuter based model of two-dimensional cardiac electrical activity," Int. J. Bifurcation Chaos Appl. Sci. Eng., 1 (1991), pp. 431-444.

[5] S. Del Pino and O. Pironneau, "A fictitious domain based general PDE solver," in Numerical methods for scientific computing. Variational problems and applications, Y. Kuznetsov, P. Neittanmaki and O. Pironneau (Eds.), CIMNE, Barcelona, 2003.

[6] M. Dumett and J. P. Keener,"A numerical method for solving anisotropic elliptic boundary value problems in 3D," SIAM J. Sci. Comput. (USA) 25 (2003), pp. 348-367.

[7] F.H. Fenton, E.M. Cherry, H.M. Hastings, and S. J. Evans, "Multiple mechanisms of spiral wave breakup in a model of cardiac electrical activity," Chaos, 12 (2002), pp. 852-892 .

[8] F.H. Fenton, E.M. Cherry, A. Karma, W.-J. Rappel, "Modeling wave propagation in realistic heart geometries using the phase-field method", Chaos, 15 (2005), 013502.

[9] F.H. Fenton and A. Karma, "Vortex dynamics in three-dimensional continuous myocardium with fiber rotation: Filament instability and fibrillation," Chaos, 8 (1998), pp. 20-47.

[10] A. Fogelson and J. P. Keener, "Immersed interface methods for Neumann and related problems in two and three dimensions," SIAM J. Sci. Comput. (USA) 22 (2001), pp. 1630-1654.

[11] J. J. Fox, J. L. McHarg, and R. F. Gilmour, "Ionic mechanism of electrical alternans," Am. J. Physiol. 282 (2002), pp. 516-530.

[12] R.L. Graham, D.E. Knuth, O. Patashnik, Concrete Mathematics, 2nd edition, Addison-Wesley, Boston, 1994.

[13] D. Harrild and C. Henriquez, "A computer model of normal conduction in the human atria," Circ. Res. 87 (2000), pp. 25-36.

[14] A. Karma, "Spiral breakup in model equations of action potential propagation in cardiac tissue," Phys. Rev. Lett., 71 (1993), pp. 1103-1106.

[15] A. Karma and W.-J. Rappel, "Quantitative phase-field modeling of dendritic growth in two and three dimensions," Phys. Rev. E 57 (1998), pp. 4323-4349.

[16] R. Leveque and D. Calhoun, "Cartesian grid methods for fluid flow in complex geometries," Computational modeling in biological fluid dynamics, L. Fauci, S. Gueron (eds.), Springer-Verlag, New York, 2001, pp 117-144.

[17] M. Lorange and R. M. Gulrajani, "Computer simulation of the Wolff Parkinson-White preexcitation syndrome with a modified Miller Geselowitz heart model," IEEE Trans. Biomed. Eng., 33 (1986), pp. 862-873.

[18] J. M. Meunier, J. C. Eason, and N. A. Trayanova, "Termination of reentry by a long-lasting AC shock in a slice of canine heart: a computational study," J. Cardiovasc. Electrophysiol. 13 (2002), pp. 1253-1261.

[19] C. Moler and C. Van Loan, "Nineteen dubious ways to compute the exponential of a matrix, twenty-five years later," SIAM Review, 45 (2003), pp. 3-49.

[20] P. M. Nielsen, I. J. Le Grice, B. H. Smaill, and P. J. Hunter, "Mathematical model of

geometry and fibrous structure of the heart," Am. J. Physiol., 260 (1991), pp. 1365-1378.

[21] M. Okajima, T. Fujino, T. Kobayashi, and K. Yamada, "Computer simulation of the propagation process in excitation of the ventricles," Circ. Res., 23 (1968), pp. 203-211.

[22] A. V. Panfilov and J. P. Keener, "Re-entry in an anatomical model of the heart," Chaos, Solitons Fractals 5 (1995), pp. 681-689.

[23] R. Plonsey and R. C. Barr, Bioelectricity: A Quantitative Approach, Plenum, New York, 1988.

[24] M. Potse, B. Dube, J. Richer; A. Vinet, and R.M. Gulrajani, "A Comparison of Monodomain and Bidomain Reaction-Diffusion Models for Action Potential Propagation in the Human Heart," IEEE Trans. BME, 53 (2006) pp. 2425-2435.

[25] W. Reinboldt, J. A. Abildkov, R. S. Ledley, and A. E. Oestreich, "Simulation of the ventricles of the heart," Proceedings of the 16th Annual Conference on Engineering in Medicine and Biology 3233 (1963).

[26] J.M. Rogers, "Wave front fragmentation due to ventricular geometry in a model of the rabbit heart," Chaos, 12 (2002), pp. 779-787.

[27] R. Sidje, "Expokit: A Software Package for Computing Matrix Exponentials," ACM Trans. Math. Softw., 24 (1998), pp. 130-156. Software available at http://www.maths.uq.edu.au/expokit/.

[28] F. J. Vetter and A. D. McCulloch, "Three-dimensional analysis of regional cardiac function: a model of rabbit ventricular anatomy," Prog. Biophys. Mol. Biol. 69 (1998), pp. 157-183.

[29] F. J. Vetter and A. D. McCulloch, "Three-dimensional stress and strain in passive rabbit left ventricle: a model study," Ann. Biomed. Eng. 28 (2000), pp. 781-792.

[30] F. Xie, Z. Qu, J. Yang, A. Baher, J. N. Weiss, and A. Garfinkel, "A simulation study of the effects of cardiac anatomy in ventricular fibrillation," J. Clin. Invest. 113 (2004), pp. 686-693.

[31] A. Yamanaka, K. Okazaki, S. Urushibara, M. Kawato, and R. Suzuki, "Reconstruction of electrocardiogram using ionic current models for heart muscles," Jpn. Heart J., 27 (1986), pp. 185-193.